Chinese Chemical Letters 36 (2025) 109891

Contents lists available at ScienceDirect

Chinese Chemical Letters

journal homepage: www.elsevier.com/locate/cclet

Spin-orbit-controlled metal-insulator transition in metastable $SrIrO_3$ stabilized by physical and chemical pressures

Jinjin Yang[a], Chuanhui Zhu[a,*], Shuang Zhao[a], Tao Xia[a], Pengfei Tan[a], Yutian Zhang[a], Mei-Huan Zhao[a], Yijie Zeng[b], Man-Rong Li[a,c,*]

[a] Key Laboratory of Bioinorganic and Synthetic Chemistry of Ministry of Education, School of Chemistry, Sun Yat-sen University, Guangzhou 510006, China
[b] College of Science, Hangzhou Dianzi University, Hangzhou 310018, China
[c] School of Chemistry and Chemical Engineering, Hainan University, Haikou 570228, China

ARTICLE INFO

Article history:
Received 24 January 2024
Revised 9 April 2024
Accepted 15 April 2024
Available online 30 April 2024

Keywords:
Chemical pressure
Spin-orbit coupling
Metal-insulator-transition
Magnetoresistance
Iridate

ABSTRACT

Spin-orbit coupling (SOC) plays a vital role in determining the ground state and forming novel electronic states of matter where heavy elements are involved. Here, the prototypical perovskite iridate oxide $SrIrO_3$ is investigated to gain more insights into the SOC effect in the modification of electronic structure and corresponding magnetic and electrical properties. The high pressure metastable orthorhombic $SrIrO_3$ is successfully stabilized by physical and chemical pressures, in which the chemical pressure is induced by Ru doping in Ir site and Mg substitution of Sr position. Detailed structural, magnetic, electrical characterizations and density functional theory (DFT) calculations reveal that the substitution of Ru for Ir renders an enhanced metallic characteristic, while the introduction of Mg into Sr site results in an insulating state with 10.1% negative magnetoresistance at 10 K under 7 T. Theoretical calculations indicate that Ru doping can weaken the SOC effect, leading to the decrease of orbital energy difference between $J_{1/2}$ and $J_{3/2}$, which is favorable for electron transport. On the contrary, Mg doping can enhance the SOC effect, inducing a metal-insulator-transition (MIT). The electronic phase transition is further revealed by DFT calculations, confirming that the strong SOC and electron-electron interactions can lead to the emergence of insulating state. These findings underline the intricate correlations between lattice degrees of freedom and SOC in determining the ground state, which effectively stimulate the physical pressure between like structures by chemical compression.

Unlike 3d or 4d electrons, 5d electrons are significantly different due to the radial distribution function and strong spin-orbit coupling (SOC) effect [1-9]. The strong SOC of 5d electrons drives energy level splitting to generate new electronic states, which interact with spatial and temporal symmetry breaking, delivering new quantum effects and functionalities in the large class of perovskite materials, such as spin Hall effect [10-12], Weyl semimetal [13-15], Rashba effect [16-18], topological surface states [19], and magnetic skyrmion [20,21]. The representative 5d compounds, perovskite iridates, have garnered significant interest in SOC system. Particularly, Ruddlesden-Popper iridates $Sr_{n+1}Ir_nO_{3n+1}$ display metal-insulator transition (MIT) driven by the modulation of bandwidth, from strongly insulating Sr_2IrO_4 to metallic non-Fermi liquid $SrIrO_3$ [22-24]. Of special interest is the strong SOC combined with the modest electronic correlations, leading to a novel spin-orbital Mott insulator with a $J_{1/2}$ ground state [25,26]. Thus, a slightly perturbation can affect the stability of insulating phase, such as defect [27], carrier doping [28], magnetic field [29], or external pressure [30-33]. For example, $Sr_2Ir_{1-x}T_xO_4$ (T = Ru, Rh) provides the first demonstration of a spin-orbit-controlled MIT phenomenon [34], which is consistent with theoretical calculations in the finite SOC systems Sr_2IrO_4 ($n=1$) [35-37]. In addition, the spin-orbit Mott insulator $Sr_3Ir_2O_7$ ($n=2$), a double-layered perovskite, provides a valuable platform to explore the collapse of Mott gap under high pressure (HP) [38]. At 59.5 GPa, $Sr_3Ir_2O_7$ transforms into a confined metal, exhibiting metallicity in the *ab* plane but insulating behavior along the *c* axis, which is similar to the peculiar metal phase observed in cuprate superconductors. A small amount of La substitution for Sr in $(Sr_{1-x}La_x)_3Ir_2O_7$ can also melt away its insulating gap, and thus lead to a correlated-metallic state [39]. These findings emphasize the intricate correlation between SOC and MIT.

Metastable orthorhombic $SrIrO_3$ (denoted as *O*-$SrIrO_3$, space group of *Pnma*) is the end member of the Ruddlesden-Popper

* Corresponding authors.
E-mail addresses: zhuchh6@mail2.sysu.edu.cn (C. Zhu), limanrong@mail.sysu.edu.cn (M.-R. Li).

https://doi.org/10.1016/j.cclet.2024.109891
1001-8417/

$Sr_{n+1}Ir_nO_{3n+1}$ series with n being infinite, which is prepared under HP (5.0 GPa) [40,41]. Nevertheless, the thermodynamically stable phase of $SrIrO_3$ is in monoclinic structure (named as 6*H*-$SrIrO_3$, space group of $C2/c$) prepared at atmospheric pressure (AP) [42]. The SOC and electronic correlation in $SrIrO_3$ polymorphs manifest interesting magnetic and electrical properties, providing an ideal platform for chemical/electronic structure-dependent phase engineering. Previous studies have demonstrated that the 6*H*-$SrIrO_3$ exhibits metallic conductivity with non-Fermi-liquid behavior, being the first known paramagnet in ternary iridate oxides [43]. The *O*-$SrIrO_3$ also exhibits paramagnetic (PM) behavior and metallic response with a MIT near 44 K with a positive magnetoresistance (MR) effect at low temperature, where the metallic property is likely due to the large electron hopping [44]. The 6*H*-$SrIrO_3$ can be destabilized by partial Ir substitution with larger size and less electronegative cations (such as Li, Mg, Fe, Co, Ni, Zn) by the alteration of electron interactions, resulting in the *O*-$SrIrO_3$ polymorph under AP [45]. It is noteworthy that, the uneven distribution of electrons in the degenerate 5d orbital (t_{2g} or e_g) of the central ion would lead to the distortion of IrO_6 octahedra, which can be altered by crystal field splitting regulation. Thus, *O*-$SrIrO_3$ provides a fascinating playground to explore MIT driven by intertwined charge, spin, and lattice degrees of freedom. For example, the Dirac semi-metal state ($x=0$) of $SrIr_{1-x}Sn_xO_3$ can be suppressed by the locally interposed Sn^{4+} ($4d^{10}$), leading to an antiferromagnetic (AFM) insulator ground state [46]. The orbital inactive Sn^{4+} ($4d^{10}$) predominantly promotes the Mott localization of the $J_{1/2}$ state by reducing the effective one-electron bandwidth, while that of $J_{3/2}$ state is merely moderately changed. Nevertheless, the former attempts at revealing that the role of SOC in *O*-$SrIrO_3$ have been hindered by concurrently occurring changes to the filling, thus the direct evidence for the role of SOC in stabilizing the insulating state still remains unclear, where the novel MIT is potentially driven by alteration of the bandwidth for $J_{1/2}$ and $J_{3/2}$ states.

To address these concerns, we realize the preservation of metastable *O*-$SrIrO_3$ polymorph by employing physical and chemical pressures, where the chemical pressure is driven by Ru and/or Mg doping into Ir and Sr site, respectively. Comprehensive characterizations on the crystal structure, magnetic and electrical properties and DFT calculations reveal that Ru doping weakens the SOC to support metallic state, and Mg doping enhances the SOC with modest electron-electron correlations to stabilize insulating state, manifesting SOC controlled MIT.

The phase transition from 6*H*- to *O*-$SrIrO_3$ can be initiated by elevated physical pressure (prepared at 5.0 GPa and 1273 K). The purity of two different polymorphs is firstly investigated by powder X-ray diffraction (PXD) measurements (Fig. S1a in Supporting information). Rietveld refinements of PXD data of 6*H*-$SrIrO_3$ in monoclinic $C2/c$ symmetry is displayed in Fig. S1b (Supporting information). The target HP sample is further investigated using synchrotron PXD (SPXD) measurements, which intensify the identification of crystalline structure (Fig. S2a in Supporting information). Tables S1 and S2 (Supporting information) show that crystallographic information including selected interatomic distances, bond angles and bond valence sums (BVS). As a rule of thumb, the structure of ABO_3 compounds can be predicted from the ionic radii by the Goldschmidt tolerance factor, $t=(r_A+r_O)/\sqrt{2}(r_B+r_O)$ [47]. When t is close to 1, cubic symmetry is expected, and distortions from the ideal cubic structure to tetragonal, orthorhombic and monoclinic symmetries are anticipated for lowering t values. As for $SrIrO_3$, $t=0.992$ indicate a cubic or *pseudo*-cubic symmetry. Nevertheless, the thermodynamically stable phase of $SrIrO_3$ adopts distorted monoclinic 6*H* polymorph, which is very unusual for ABO_3 with t around 1. Fig. 1a schematically describes the crystal structure of 6*H*-$SrIrO_3$, in which corner-shared $Ir(1)O_6$ octahedra and $Ir(2)_2O_9$ dimers formed by two face-sharing $Ir(2)O_6$ octahedra

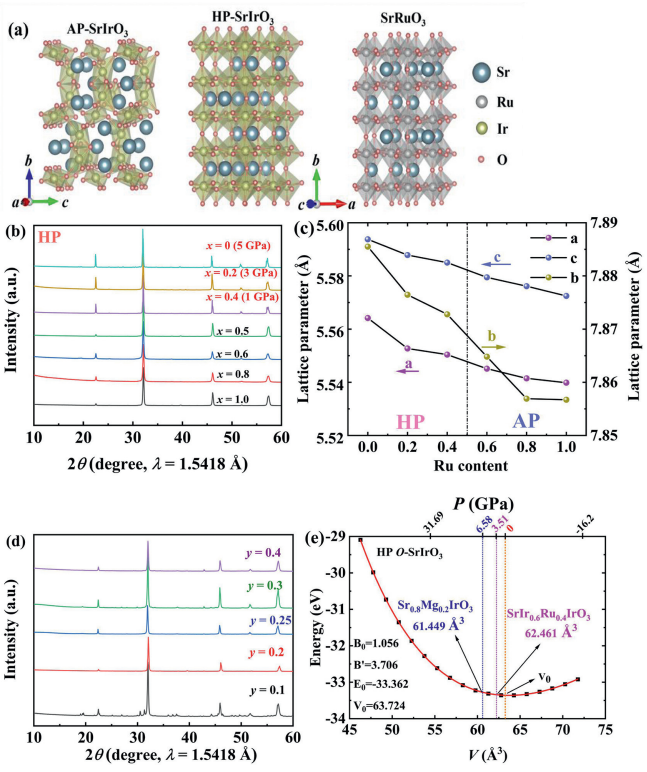

Fig. 1. (a) Comparison of the crystal structures in monoclinic $C2/c$, orthorhombic *Pnma* of $SrIrO_3$ and *Pnma*-$SrRuO_3$. (b) PXD patterns of $SrIr_{1-x}Ru_xO_3$ ($0\le x\le 1.0$) prepared by solid-state reaction combined with high-temperature and high-pressure synthesis. (c) x dependence of lattice parameter a (Å), b (Å) and c (Å) in orthorhombic $SrIr_{1-x}Ru_xO_3$ ($0\le x\le 1.0$) refined from SPXD data. (d) PXD patterns of $Sr_{1-y}Mg_yIrO_3$ ($y=0$–0.4) prepared by solid-state reaction at AP. (e) *E*-*V* curve of HP *O*-$SrIrO_3$ to show the equivalent chemical pressure by Ru or Mg doping.

are alternatively arranged along the c direction, giving a *cchcch* stacking sequence. The Ir(2)-Ir(2) distances across face sharing octahedra are relatively short (~2.75 Å), implying strong metal-metal bonding and stretched Ir(2)-O bond within the highly distorted octahedral dimers in 6*H*-$SrIrO_3$. Owing to the subtle balance between strong Ir-Ir bonding and Coulombic repulsion across the face-sharing octahedra, a reconstructive phase transition would be ignited in 6*H*-$SrIrO_3$ when dwelled under HP (5.0 GPa) and high temperature, giving the metastable orthorhombic structure contained only corner-sharing IrO_6 octahedra (Fig. 1a). Despite the slight difference in ionic radii of Ir^{4+} ($r_{Ir}\sim 0.625$ Å) and Ru^{4+} ($r_{Ru}\sim 0.62$ Å), $SrRuO_3$ ($t=0.994$) crystallizes in orthorhombic symmetry isostructural to the HP *O*-$SrIrO_3$ (Fig. 1a). Obviously, the ionic size dependent geometric factor is insufficient to judge the crystal structure of $SrIrO_3$. This abnormal phenomenon emphasizes the intricate correlation between SOC (~0.4 eV for iridates and ~0.15 eV for ruthenates) and lattice.

In contrast to physical pressure, "chemical compression" (also known as chemical pressure, can be induced by substitution with smaller ion to simulate the lattice contraction under external HP) offers a feasible route to mimic the effect of external physical pressure [28,48-50]. There are two main functions of chemical pressure: structural and electronic effects. The former one alters the crystal structure, such as bond length and bond angle, while the latter route can adjust the electronic configuration of *B*-site ions by isovalent/aliovalent substitution. Both effects can modulate the structure and properties of materials, particularly in the strong correlated 5d systems, where additional SOC effect renders enriched behaviors. Accordingly, replacing Ir^{4+} by Ru^{4+} in 6*H*-$SrIrO_3$ is expected to intercept the metastable *O*-$SrIrO_3$ phase at AP. As shown

in Fig. S1c (Supporting information), single-phase solid solutions in the metastable orthorhombic structure of $SrIr_{1-x}Ru_xO_3$ ($0 \le x \le 0.5$) can be prepared by substituting Ru^{4+} ($4d^4$) for Ir^{4+} ($5d^5$) with solid-solution limit of 50%, which is largely ascribed to the key role of SOC. At high-temperature and high-pressure reaction, the solid-solution limit can be further improved, and finally single-phase solid solution with a full proportion can be prepared below 5.0 GPa (Fig. 1b). The refined crystallographic information from SPXD data (Fig. S2 in Supporting information) are listed in Tables S1 and S2. As shown in Fig. 1c, the substituting Ru^{4+} for Ir^{4+} results in a monotonically decreasing trend in the unit cell parameters (*a*, *b*, and *c*) with increasing Ru content *x*, which together with the linear decrease of the *B*-O bond lengths and increase of the *B*-O-*B* bond angles, underlying the alteration of physical properties.

Apart from smaller *B*-site doping, substituting smaller size Mg^{2+} ($^{VIII}r_{Mg} = 0.89$ Å) for Sr^{2+} ($^{VIII}r_{Sr} = 1.26$ Å) on *A*-sites also evokes lattice contraction (chemical pressure), which is expected to destabilize the monoclinic *C*2/*c* symmetry and induce a phase transition to the orthorhombic *Pnma* symmetry in $Sr_{1-y}Mg_yIrO_3$ as displayed in Fig. 1d. $Sr_{1-y}Mg_yIrO_3$ crystallizes in the individually orthorhombic structure with Mg at 20% ($Sr_{0.8}Mg_{0.2}IrO_3$) according to refined crystallographic information from PXD data in Fig. S1d (Supporting information), which corroborates an orthorhombic *Pnma* structure. Further increasing of Mg^{2+} content ($y \ge 25\%$) results in the appearance of MgO impurity. In order to evaluate the chemical pressure stemming from volumetric difference between HP *O*-$SrIrO_3$ and the $Sr_{0.8}Mg_{0.2}IrO_3$ solid solution, the energy-volume (*E*-*V*) curve is calculated by the Murnaghan equation of state equations (Eqs. S1-S3 in Supporting information). The detailed results are shown in Fig. 1e, which indicates equivalent pressure up to 6.58 GPa for $Sr_{0.8}Mg_{0.2}IrO_3$ and 3.51 GPa for $SrIr_{0.6}Ru_{0.4}IrO_3$, further confirming the feasible trapping of metastable phase with chemical pressure at AP. Assisted by chemical pressure, simultaneous co-doping smaller ionic radii Mg^{2+} and Ru^{4+} in the Sr^{2+} and Ir^{4+} sites can further increase the solid solution limit at AP, to easier synthesize the *O*-$SrIrO_3$ than the solely electron-doped approach in $SrIr_{1-x}Ru_xO_3$, seeing PXD diagram with 10% and 20% Mg content in Figs. S3 and S4 (Supporting information). While 20% Mg^{2+} doping at *A*-site, the full solid solution by Ru substitution can be obtained at AP. So, chemical pressure over the Ru/Ir sublattice can partially stabilize the *O*-$SrIrO_3$ type solid solution in a limited chemical space when the *A*-site compression is simultaneously applied, yielding the HP polymorph in $Sr_{1-y}Mg_yIr_{1-x}Ru_xO_3$ ($0 \le y \le 0.2$; $0 \le x \le 1.0$) models.

Ru and/or Mg doping is expected to induce pronounced changes in a wide range of magnetic properties of single-phase $Sr_{1-y}Mg_yIr_{1-x}Ru_xO_3$ ($0 \le y \le 0.2$; $0 \le x \le 1.0$). The Ru doping induces obvious changes in a wide range of *M* (*T*) of $SrIr_{1-x}Ru_xO_3$ ($0 \le x \le 1.0$) with zero-field-cooling (ZFC) and field-cooling (FC) curves (Fig. 2a). The hysteresis loops *M* (*H*) of all series at different temperatures under magnetic field between −5 T and 5 T are shown in Figs. S5, S6a and b (Supporting information). Initial negative magnetization on some ZFC curves could be caused by negative trapped fields inside a magnetometer or the sample insertion procedure [51,52]. Previous studies have demonstrated that $SrRuO_3$ shows ferromagnetic (FM) ordering with Curie temperature (T_C) ~160 K [53], and *O*-$SrIrO_3$ exhibits metallic conductivity and Pauli PM [4]. In orthorhombic samples with $x = 0$, 0.2, 0.4 (synthesized at HP), there are no obvious deviation between ZFC and FC curves, indicating the basic PM. With an increase of the Ru dopant, the $x = 0.6$, 0.8, 1.0 (synthesized at AP) cases exhibit FM ordering with rising T_C at 61.2, 112.9, and 160.2 K and effective magnetic moment μ_{eff} ~ 2.37, 2.41 and 2.59 μ_B, respectively (Table S3 in Supporting information), which attributed to the Ru^{4+} at Ir^{4+} site involved in the long-range magnetic order with strengthened *B*-O-*B* exchange interaction. Fig. S7a (Supporting information) vividly

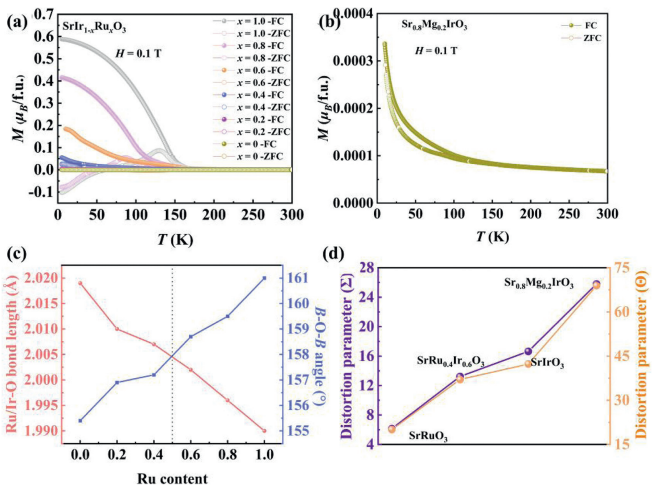

Fig. 2. Temperature-dependent magnetization of (a) $SrIr_{1-x}Ru_xO_3$ ($0 \le x \le 1.0$) and (b) $Sr_{0.8}Mg_{0.2}IrO_3$ in ZFC/FC at 0.1 T between 10 K and 300 K. (c) The evolution of *B*-O bond lengths and *B*-O-*B* bond angles in $SrIr_{1-x}Ru_xO_3$ ($0 \le x \le 1.0$). (d) BO_6 octahedron distortion (Σ and Θ) of orthorhombic $SrRuO_3$, $SrIr_{0.6}Ru_{0.4}O_3$, $SrIrO_3$ and $Sr_{0.8}Mg_{0.2}IrO_3$.

shows the trend of T_C and μ_{eff} evolution. With the increase of Ir content, the μ_{eff} and T_C of $SrIr_{1-x}Ru_xO_3$ ($0 \le x \le 1.0$) series gradually decreased, indicating that the introduction of Ir can weaken the exchange of adjacent ions. As for the solely Mg dopant in Sr^{2+} site case, $Sr_{0.8}Mg_{0.2}IrO_3$ ($y = 0.2$) captures the orthorhombic single phase and keeps PM similar to *O*-$SrIrO_3$ (Fig. 2b, Figs. S6c and d in Supporting information). It is worth noting that there is obvious deviation between ZFC and FC data, which can be attributed to spin glass-like or short-range ordering transitions. In the case of Ru and Mg co-doped $Sr_{1-y}Mg_yIr_{1-x}Ru_xO_3$ series, the FM ordering can be further enhanced with the increase of Ru content (Figs. S7bc and S8 in Supporting information).

In light of the orthorhombic structure, the distance between the *B*-site ions within the corner-shared BO_6 octahedra ranges from 3.92 Å ($SrRuO_3$) to 3.94 Å ($SrIrO_3$). Thus, the strength of the magnetic exchange interactions is expected to be governed by the *B*-O-*B* exchange interactions through the bridging O sites, which can be reflected by the evolution of *B*-O-*B* angle (Fig. 2c). In $SrIr_{1-x}Ru_xO_3$ ($0 \le x \le 1.0$), the *B*-O-*B* angle increases linearly with increasing *x* and closer to nearly 180° for $x = 1.0$, leading to a less distorted lattice with enhanced magnetic super-exchange coupling (Fig. 2d), where the symbols Σ and Θ represent the summation of deviations from of 6 and 24 distinct θ angles in the octahedra, respectively [54,55]. In $Sr_{0.8}Mg_{0.2}IrO_3$, the substitution of Mg^{2+} for Sr^{2+} leads to the change of ionic potential at *A* site with the altered Sr/Mg-O and Ir-O bond lengths and Ir-O-Ir bond angles, giving rise to larger distortion of the IrO_6 octahedra, and weakening the super-exchange interactions between adjacent electronic spins of Ir-Ir cations (AFM interaction). The measured PM properties agree well with the expected electronic exchange interactions in these orthorhombic iridates.

The measurements of electrical properties are further executed to uncover the effect of local crystal structure on the electronic transport behavior. The temperature-dependent resistivity ρ (*T*) curves measured at zero-field of representative cases are shown in Fig. 3a. Clearly, the metallic state of *O*-$SrIrO_3$, $SrIr_{0.6}Ru_{0.4}O_3$ and $SrRuO_3$ are maintained, where the resistivity values decrease with the increase of doping amount of Ru^{4+}. In contrast, the isostructural $Sr_{0.8}Mg_{0.2}IrO_3$ exhibits semiconducting behavior, which is radically different from metallic *O*-$SrIrO_3$, indicating the appropriate level of Mg^{2+} dopant at Sr^{2+} site can induce an exotic MIT in *O*-$SrIrO_3$. In addition, compared with the metallic Mg-

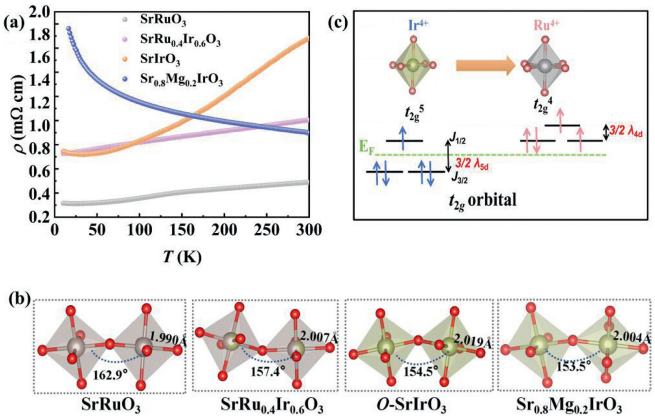

Fig. 3. (a) Temperature dependence of the resistivity of $SrRuO_3$, $SrIr_{0.6}Ru_{0.4}O_3$, *O*-$SrIrO_3$ and $Sr_{0.8}Mg_{0.2}IrO_3$ between 10 K and 300 K. (b) Local crystal structure of $SrRuO_3$, $SrIr_{0.6}Ru_{0.4}O_3$, *O*-$SrIrO_3$ and $Sr_{0.8}Mg_{0.2}IrO_3$. (c) Schematic of $Ir^{4+}$and Ru^{4+} t_{2g} orbital distribution.

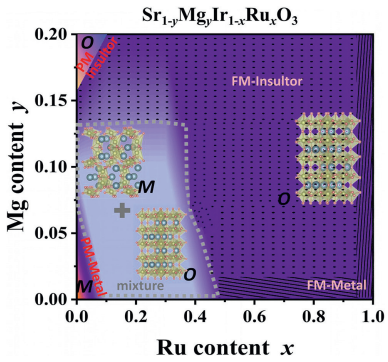

Fig. 4. Dopant-dependent structure-property phase diagram of $Sr_{1-y}Mg_yIr_{1-x}Ru_xO_3 (0 \le y \le 0.2;\ 0 \le x \le 1.0)$. *M* and *O* stand for the monoclinic and orthorhombic phase, respectively.

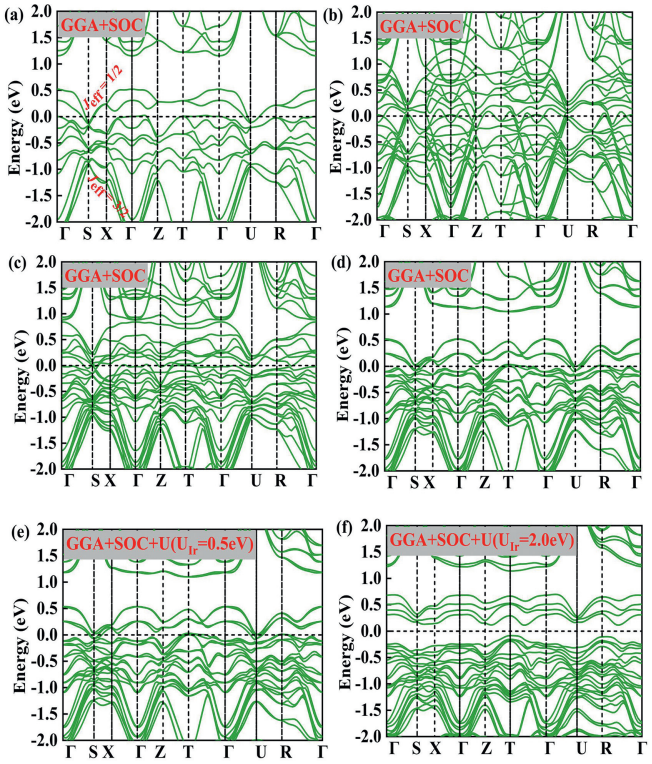

Fig. 5. The magnified view of band structure near E_F of (a) *O*-$SrIrO_3$, (b) $SrRuO_3$, (c) $SrIr_{0.6}Ru_{0.4}O_3$ and (d) $Sr_{0.8}Mg_{0.2}IrO_3$ from GGA+SOC method. And band structure near E_F of $Sr_{0.8}Mg_{0.2}IrO_3$ from GGA+SOC+U method as $U_{eff\,(Ir)}$ = (e) 0.5, (f) 2.0 eV.

free case $SrIr_{1-x}Ru_xO_3$, the series of Mg doped $Sr_{0.9}Mg_{0.1}Ir_{1-x}Ru_xO_3$ $(0.4 \le x \le 1.0)$ and $Sr_{0.8}Mg_{0.2}Ir_{1-x}Ru_xO_3$ $(0 \le x \le 1.0)$ all transform into semiconducting response except for samples containing only Ru at the *B* site as shown in Figs. S9a and b (Supporting information). The corresponding phase diagram of magnetic and electrical properties related to Mg^{2+} and Ru^{4+} doping levels is depicted in Fig. 4, exhibiting interesting magnetic and electrical variations. In particular, the MIT phenomenon due to the doping of Mg at Sr site is highlighted.

To assess the origin of the MIT in the orthorhombic iridates, the local crystal structure evolution of corner-shared BO_6 octahedra of representative samples are schematically described in Fig. 3b. Clearly, the angles of *B*-O-*B* decrease from 162.9° ($SrRuO_3$), 157.4° ($SrIr_{0.6}Ru_{0.4}O_3$), 154.5° (*O*-$SrIrO_3$) to 153.5° ($Sr_{0.8}Mg_{0.2}IrO_3$), indicating a stronger $GdFeO_3$-type distortion of the IrO_6 octahedra by Mg substitution for Sr. The crystal field and SOC are deterministic of the electronic structure of the $5d^5$ (Ir^{4+}) and $4d^4$ (Ru^{4+}) distribution (Fig. 3c). In $5d^5$ (Ir^{4+}) orbital, four out of five d electrons occupy the $J_{eff} = 3/2$ state, leaving one electron in the $J_{eff} = 1/2$ state. In $4d^4$ (Ru^{4+}) orbital, three out of four d electrons occupy the $J_{eff} = 3/2$ state, leaving one electron in the $J_{eff} = 1/2$ state. Thus, Ru doping, which has one more hole than Ir, would reduce the magnitude of the SOC and structural distortion, and add holes to the t_{2g} orbit.

To gain more insight on the correlations between SOC and ground state in the iridates, DFT calculations are further performed to elucidate the effect of SOC on electrical transport property when Ru and Mg are doped in *O*-$SrIrO_3$. The band structure of *O*-$SrIrO_3$ subjected to SOC is shown in Fig. 5a. For iridate Ir^{4+} ($5d^5$), the stronger SOC leads to the $J_{1/2}$ and $J_{3/2}$ with a large energy difference $\lambda_{5d} \sim 0.47$ eV, which is in line with $\lambda_{5d} \sim 0.43$ eV in *O*-$SrIrO_3$ from DFT+*U* method with $U_{eff\,(Ir)} = 0$ eV [56]. Conversely, Ru^{4+} ($4d^4$) with weaker SOC manifests small energy difference ($\lambda_{4d} \sim 0.16$ eV) between $J_{1/2}$ and $J_{3/2}$, as the band structure of $SrRuO_3$ subjected to SOC shown in Fig. 5b. Here, $SrIr_{0.6}Ru_{0.4}O_3$ is opted as a reasonable structure model, which can intensify the understanding of the influence on SOC effects with Ru doping. The band structure of $SrIr_{0.6}Ru_{0.4}O_3$ subjected to SOC is shown in Fig. 5c. The competition between SOC interaction and Hund's effect leads to diluted SOC in Ir site in $SrIr_{0.6}Ru_{0.4}O_3$ compared to that in *O*-$SrIrO_3$. Thus, the weaker SOC combined with more effectively screened coulomb interactions between O 2p and Ru/Ir 4d/5d electrons can cause reduction of t_{2g} orbital difference and lower E_F, driving to the system toward a more robust metallic state. This is consistent with the above electronic transport measurements. As for the computing model of $Sr_{0.8}Mg_{0.2}IrO_3$, a supposed *O*-$SrIrO_3$ with 20% Mg dopant concentration in Sr sites is constructed. The band structure of $Sr_{0.8}Mg_{0.2}IrO_3$ subjected to SOC is shown in Fig. 5d. The stronger $GdFeO_3$-type distortion induces $J_{1/2}$ and $J_{3/2}$ states further splitting due to enhanced SOC. Compared with *O*-$SrIrO_3$, $Sr_{0.8}Mg_{0.2}IrO_3$ exhibits further energy level splitting induced by the finite coulomb repulsion energy *U* (~0.1 eV). Moving down the periodic table from 3d to 4d and then to 5d, the orbitals in the solids that contain the corresponding d orbitals become increasingly extended and so does the bandwidth ($W_{3d} < W_{4d} < W_{5d}$). As the bandwidth increases, the corresponding on-site Coulomb repulsion decreases in a sequential manner ($U_{3d} > U_{4d} > U_{5d}$) [57]. So, the 5d orbits have smaller on-site Coulomb interaction *U* than the 3d and 4d orbits. Thus, the electron correlation should contribute less to the energy band structure, giving rise to the metallic ground states in many 5d transition metal oxides (TMOs) described by the band

theory of solid. However, some 5d TMOs, such as Sr_2IrO_4, $Sr_3Ir_2O_7$, and Ba_2NaOsO_6, have insulating ground states, which can be attribute to the key role of electron correlation effects *U* [58-60]. To achieve the insulating bands, the on-site Coulomb interactions *U* is considered in the Hamiltonian to drive the localization of charge carriers [61]. Thus, the band structure is further calculated combined SOC and on-site Coulomb interactions, where electron correlation $U_{eff\ (Ir)}$ values are tested from 0.5 eV to 3 eV. When the $U_{eff\ (Ir)}$ value is 0.5 and 1.0 eV, the electronic structures are metallic from GGA+SOC+*U* method (Fig. 5e and Fig. S10a in Supporting information). As the $U_{eff\ (Ir)}$ value is adjusted to 2.0 and 3.0 eV, finite indirect band gaps of 0.18 and 0.50 eV can be observed in Fig. 5f and Fig. S10 (Supporting information), respectively. It is seen that the occupied electronic states of Ir 5d electrons become isolated and localized. Thus, the band structure derived from GGA+SOC+*U* calculations is consistent with our experimental results, demonstrating that the insulator behavior can be ignited by combining SOC and the on-site Coulomb interactions. That is, electron correlation *U* and SOC effect are non-negligible factors in MIT phenomenon in DFT calculations. Electron-electron Coulomb repulsion interactions (*U*) for Ru 4d orbitals are considered in GGA+SOC+*U* method with $U_{eff\ (Ru)} = 2.9$ eV as used to predict metallic behavior of $SrRuO_3$ [62]. When the $U_{eff\ (Ir)}$ value is 2.0 eV and $U_{eff\ (Ru)}$ value is 2.9 eV, the electronic structure is metallic from GGA+SOC+*U* method (Fig. S11 in Supporting information) in $SrIr_{0.6}Ru_{0.4}O_3$ case, which aligns with our experimental observations, confirming the existence of metallic behavior in the context of Ru doping. All in all, the ground state in strong correlated 5d elements systems is governed by the cooperative effect involving SOC, electron-electron correlations, and crystal field effect, which are expected to raise exotic physical properties in strong correlated iridate oxides.

Bond-angle distortion in transition-metal ABO_3 perovskites would reduce the effective d-electron hopping energy and/or the electron bandwidth, *via* the reduced hybridization between transition-metal d and oxygen p states. In fact, the variation of bond angle with the change of *A*-site ionic size occasionally causes drastic electronic changes, such as the bandwidth-controlled Mott transition and the colossal MR. The metastable HP *O*-$SrIrO_3$ perovskite is an exceptional compound among known iridates in terms of its unusual positive MR (PMR) effect (12% at 20 K and 7 T) [44]. To assess the influence of resistivity in $Sr_{0.8}Mg_{0.2}IrO_3$ under magnetic field, the temperature dependence of resistivity is measured at 7.0 T. As shown in Fig. 6a, the resistivity decreases with applied magnetic field, indicating negative MR (NMR) effect. According to the relationships of MR [$MR = (\rho_H - \rho_0)/\rho_0$] and temperatures, we consequently investigate the NMR in the orthorhombic $Sr_{0.8}Mg_{0.2}IrO_3$ perovskite (Fig. 6b), giving maximum NMR (−10.1%) at 10 K under 7 T. In general, a variety of MR behavior can be observed by changing the temperature, magnetic field, doping level, and so on. Therein, the NMR is induced by the reduction of scattering and field suppression of localization, while the PMR can be arising from Zeeman spin splitting and spin-orbit scattering [63,64]. In the orthorhombic $Sr_{0.8}Mg_{0.2}IrO_3$, NMR at low temperatures can be ascribed to the reduced scattering ignited by disorder-induced localization under magnetic field. Due to the p-d exchange in Mg-doped *O*-$SrIrO_3$ system, charge carrier is surrounded by the polarized magnetic ion electron cloud, thus the spin magnetic moment will be arranged in parallel with the direction of external magnetic field, leading to the enhancement of charge carrier mobility. Therefore, the resistivity will decrease with the increase of magnetic field. As temperature increases, the magnetic moment alignment is gradually disordered due to intensified thermal motion of the molecules, leading to the decrease of NMR. Similar phenomenon has been reported in other oxides [65-67]. The NMR of $Sr_{0.8}Mg_{0.2}IrO_3$ tends to be stable above 150 K, which can be attributed to reduced effect of magnetic field on electron scattering, resulting in a weakened temperature dependence of MR.

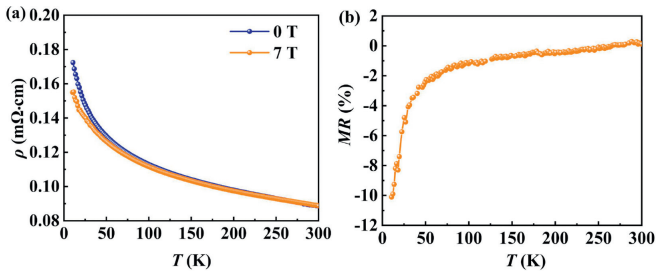

Fig. 6. Temperature dependence of the (a) resistivity and (b) MR of $Sr_{0.8}Mg_{0.2}IrO_3$ between 10 K and 300 K measured at 0 and 7 T.

In conclusion, we have captured metastable orthorhombic *O*-$SrIrO_3$ by both physical and chemical pressures, and investigated the correlation between lattice and SOC in determining the ground state in SOC system. In chemical pressure strategy, $Sr_{1-y}Mg_yIr_{1-x}Ru_xO_3$ with Ru^{4+} doped in Ir^{4+} site and/or Mg^{2+} doped in Sr^{2+} sites can stabilize the orthorhombic metastable *O*-$SrIrO_3$ phase. The Ru-doping keeps ferromagnetic metallic state, while the Mg-dopant successfully traps paramagnetic semiconducting state with NMR compared to the pristine paramagnetic and metallic *O*-$SrIrO_3$ with PMR. Co-doping smaller ionic radii Mg^{2+} and Ru^{4+} in the Sr^{2+} and Ir^{4+} sites can further increase the solid solution concentration and regulate the magnetic and electrical properties. The exotic electronic phase transition is further uncovered by the DFT calculations, emphasizing the key role of cooperative effect involving SOC, electron-electron correlations, and crystal field effect in determining the ground state of these iridate oxides. The present findings provide a plausible strategy for stabilizing metastable phases by regulating electronic structure through chemical pressure.

Declaration of competing interest

The authors report no competing financial interest.

CRediT authorship contribution statement

Jinjin Yang: Writing – original draft, Writing – review & editing. **Chuanhui Zhu:** Formal analysis, Supervision, Writing – original draft, Writing – review & editing. **Shuang Zhao:** Data curation, Investigation. **Tao Xia:** Investigation. **Pengfei Tan:** Investigation. **Yutian Zhang:** Investigation. **Mei-Huan Zhao:** Investigation. **Yijie Zeng:** Methodology, Software. **Man-Rong Li:** Funding acquisition, Validation, Writing – original draft, Writing – review & editing, Supervision.

Acknowledgments

This work was financially supported by the National Natural Science Foundation of China (NSFC, No. 22090041), the Guangdong Basic and Applied Basic Research Foundation (No. 2022B1515120014).

Supplementary materials

Supplementary material associated with this article can be found, in the online version, at doi:10.1016/j.cclet.2024.109891.

References

[1] Y.N. Liu, S.F. Wang, Y.T. Tao, et al., Chin. Chem. Lett. 27 (2016) 1250–1258.
[2] Q. Cui, J.G. Cheng, W. Fan, et al., Phys. Rev. Lett. 117 (2016) 176603.

[3] S. Bhowal, I. Dasgupta, J. Phys. Condens Matter. 33 (2021) 1–42.
[4] P.E.R. Blanchard, E. Reynolds, B.J. Kennedy, et al., Phys. Rev. B 89 (2014) 214106.
[5] J.P. Clancy, N. Chen, C.Y. Kim, et al., Phys. Rev. B 86 (2012) 1–9.
[6] Y. Qi, S. Matsuishi, J. Guo, et al., Phys. Rev. Lett. 109 (2012) 217002.
[7] J. Guo, Y. Qi, S. Matsuishi, et al., J. Am. Chem. Soc. 134 (2012) 20001–20004.
[8] C. Lu, J.M. Liu, Adv. Mater. 32 (2020) 1904508.
[9] H.W. Wang, L.Y. Zhang, N. Hu, et al., Phys. Rev. Mater. 5 (2021) 104412.
[10] Y. Ohuchi, J. Matsuno, N. Ogawa, et al., Nat. Commun. 9 (2018) 213.
[11] A.S. Patri, K. Hwang, H.W. Lee, et al., Sci. Rep. 8 (2018) 8052.
[12] H.R. Fuh, B. Yan, S.C. Wu, et al., New J. Phys. 18 (2016) 113038.
[13] J.M. Kim, M.F. Haque, E.Y. Hsieh, et al., Adv. Mater 35 (2023) e2107362.
[14] X. Ou, H. Wu, et al., Sci. Rep. 4 (2014) 4609.
[15] Y. Yang, F. Yu, X. Wen, et al., Nat. Commun. 14 (2023) 2260.
[16] D. Bhowmik, L. You, S. Salahuddin, et al., Nat. Nanotechnol. 9 (2014) 59–63.
[17] D. Maryenko, M. Kawamura, A. Ernst, et al., Nat. Commun. 12 (2021) 3180.
[18] L. Zhang, Y.B. Chen, B. Zhang, et al., J. Phys. Soc. Jpn. 83 (2014) 054707.
[19] M.M. Otrokov, D.Estyunin Klimovskikh, et al., Nature 576 (2019) 416–422.
[20] K.Y. Meng, A.S. Ahmed, M. Bacani, et al., Nano Lett. 19 (2019) 3169–3175.
[21] X. Yao, J. Chen, S. Dong, et al., New J. Phys. 22 (2020) 083032.
[22] B.J. Kim, H. Jin, S.J. Moon, et al., Phys. Rev. Lett. 101 (2008) 076402.
[23] B.J. Kim, H. Ohsumi, T. Komesu, et al., Science 323 (2009) 1329–1332.
[24] S.J. Moon, H. Jin, K.W. Kim, et al., Phys. Rev. Lett. 101 (2008) 226402.
[25] L. Hao, D. Meyers, M.P.M. Dean, et al., J. Phys. Chem. Solids. 128 (2019) 39–53.
[26] I. Qasim, B.J. Kennedy, M. Avdeev, et al., J. Mater. Chem. A 1 (2013) 13357–13362.
[27] P. Tan, C. Zhu, J. Yang, et al., Chin. Chem. Lett. 35 (2023) 108485.
[28] J.L. García-Muñoz, M. Suaaidi, M.J. Martínez-Lope, et al., Phys. Rev. B 52 (1995) 13563–13569.
[29] Z.L. Sun, A.F. Wang, H.M. Mu, et al., npj Quantum Mater. 6 (2021) 94.
[30] T. Hussain, M.J. Oh, M. Nauman, et al., Phys. B: Condens. Matter. 536 (2018) 235–238.
[31] G. Duvjir, B.K. Choi, I. Jang, et al., Nano Lett. 18 (2018) 5432–5438.
[32] S. Zhao, J. Yang, Y. Han, et al., Chin. Chem. Lett. 34 (2023) 107355.
[33] M. Xi, C. He, H. Yang, et al., Chin. Chem. Lett. 33 (2022) 2595–2599.
[34] H. Wang, M. Marshall, Z. Wang, et al., Inorg. Chem. 62 (2023) 2161–2168.
[35] V. Brouet, P. Foulquier, A. Louat, et al., Phys. Rev. B 104 (2021) 121104.
[36] H. Jin, H. Jeong, T. Ozaki, et al., Phys. Rev. B 80 (2009) 075112.
[37] T.F. Qi, O.B. Korneta, L. Li, et al., Phys. Rev. B 86 (2012) 125105.
[38] P. Schutz, D. Di Sante, L. Dudy, et al., Phys. Rev. Lett. 119 (2017) 256404.
[39] V. Singh, J.J. Pulikkotil, Conference: 59th DAE-BRNS 1665 (2015) 090034.
[40] J.M. Carter, V.V. Shankar, M.A. Zeb, et al., Phys. Rev. B 85 (2012) 115105.
[41] V. Singh, J.J. Pulikkotil, J. Phys-condens. Mat. 27 (2015) 335502.
[42] J. Yu, X. Wu, D. Guan, et al., Chem. Mater. 32 (2020) 4509–4517.
[43] L. Yang, H. Chen, L. Shi, et al., ACS Appl. Mater. Interfaces 11 (2019) 42006–42013.
[44] J.G. Zhao, L.X. Yang, Y. Yu, et al., J. Appl. Phys. 103 (2008) 103706.
[45] I. Qasim, B.J. Kennedy, M. Avdeev, et al., J. Mater. Chem. A 1 (2013) 3127–3132.
[46] J. Fujioka, T. Okawa, M. Masuko, et al., J. Phys. Soc. Jpn. 87 (2018) 123706.
[47] R.A. Jishi, M.A. Lucas, Int. J. Photoenergy 2016 (2016) 1–9.
[48] R. Sun, S. Jin, J. Deng, et al., Adv. Funct. Mater. 31 (2021) 2102917.
[49] M.H. Zhao, X. Zhou, Y. Han, et al., Chem. Mater. 34 (2022) 10153–10161.
[50] X. Zhou, M.H. Zhao, J. Yang, Y, et al., Mater. Today Chem. 25 (2022) 100902.
[51] L. Zhang, N. Terada, R.D. Johnson, et al., Inorg. Chem. 57 (2018) 5987–5998.
[52] R. Liu, M. Tanaka, K. Yamaura, et al., J. Alloys Compd. 825 (2020) 154019.
[53] C. Sow, D. Samal, A.K. Bera, et al., AIP Conf. Proc. 1512 (2013) 90–91.
[54] J.A. Alonso, M.J. Martıńez-Lope, M.T. Casais, Inorg. Chem. 39 (2000) 917–923.
[55] M. Buron-Le Cointe, J. Hébert, C. Baldé, et al., Phys. Rev. B 85 (2012) 064114.
[56] A. Chauhan, B.R.K. Nanda, Phys. Rev. B 105 (2022) 045127.
[57] K. Samanta, J. Noky, I. Robredo, et al., npj Comput. Mater. 9 (2023) 167.
[58] J.M. Rondinelli, N.M. Caffrey, S. Sanvito, et al., Phys. Rev. B 78 (2008) 155107.
[59] S. Gangopadhyay, W.E. Pickett, Phys. Rev. B 91 (2015) 045133.
[60] C. Martins, M. Aichhorn, S. Biermann, J. Phys. Condens Matter. 29 (2017) 263001.
[61] W. Ju, G.Q. Liu, Z. Yang, Phys. Rev. B 87 (2013) 075112.
[62] R.D. Wulandari, S. Muhammady, Y. Darma, et al., J. Phys. Chem. Solids. 137 (2020) 109225.
[63] K. Liu, X. Ma, S. Xu, et al., npj Comput. Mater. 9 (2023) 16.
[64] G. Popov, M. Greenblatt, Phys. Rev. B 67 (2003) 024406.
[65] J. Zhao, B. Jiang, J. Yang, et al., Phys. Rev. B 107 (2023) L060408.
[66] P. Salev, L. Fratino, D. Sasaki, Phys. Rev. B 108 (2023) 174434.
[67] X. Wang, K. Huang, X. Wu, et al., Chin. Chem. Lett. 34 (2023) 108267.